Acta Materialia 234 (2022) 117996

Contents lists available at ScienceDirect

Acta Materialia

journal homepage: www.elsevier.com/locate/actamat

On the influence of Al-concentration on the fracture toughness of NiAl: Microcantilever fracture tests and atomistic simulations

Ralf Webler[a], Polina N. Baranova[a], Shivraj Karewar[a], Johannes J. Möller[a], Steffen Neumeier[a], Mathias Göken[a], Erik Bitzek[a,b,*]

[a] Friedrich-Alexander-Universität Erlangen-Nürnberg, Department for Materials Science and Engineering, Institute I, Martenstr. 5, Erlangen 91058, Germany
[b] Department of Computational Material Design, Max-Planck-Institut für Eisenforschung GmbH, Max-Planck Str. 1, Düsseldorf D-40237, Germany

ARTICLE INFO

Article history:
Received 20 September 2020
Revised 14 April 2022
Accepted 2 May 2022
Available online 8 May 2022

Keywords:
Fracture
NiAl
Intermetallics
Micro cantilever bending
Atomistic simulation

ABSTRACT

While the mechanical properties of the stoichiometric B2 β-phase of NiAl are well established, the effect of off-stoichiometric composition on the fracture behavior has not yet been systematically studied over the entire composition range of 40-55% Al. Here we use microbending tests on notched cantilever beams FIB-milled from NiAl single crystals with an aluminized as well as an oxidation-induced composition gradient to determine the influence of the Al concentration on the fracture toughness. Small variations from the stoichiometric composition are shown to lead to drastic changes in fracture behavior. Ni-rich NiAl shows a gradual decrease of fracture toughness and plastic energy dissipation with Ni-concentration that follows the inverse proportionality to the yield stress postulated by the Ritchie, Knott and Rice (RKR) model. Al-rich NiAl, however, shows a concentration-independent low fracture toughness and no signs of accompanying plasticity - both which can not be described by the RKR model. Detailed atomistic simulations show that rather than affecting the theoretical fracture toughness according to the thermodynamic Griffith criterion, structural vacancies in Al-rich NiAl lower the kinetic barrier for crack propagation, explaining the observed different concentration dependence of the fracture toughness. Similar observations are also expected for fracture in other off-stoichiometric B2 aluminides.

1. Introduction

The intermetallic phase NiAl is regarded as promising candidate material for high temperature applications because of its low density, high thermal conductivity and excellent oxidation resistance [1,2]. However, the low fracture toughness and poor ductility at room temperature as well as the comparatively low creep strength have been major obstacles towards its application as high temperature structural material [3]. NiAl, which crystallizes in the B2 (CsCl) structure, is however frequently used as a bond coat material for oxidation protection of turbine blades and vanes in aircraft engines [4]. These bond coats have a characteristic composition gradient throughout their thickness, which is believed to significantly affect their mechanical behavior and failure resistance under load [5]. Understanding the composition dependent mechanical properties of NiAl is therefore of prime importance for improving the reliability of bond coats on turbine blades and vanes.

The study of the composition dependence of fracture in intermetallic alloys is, however, also interesting from a fundamental point of view. The fracture toughness of semi-brittle materials like B2 NiAl is determined by the competition between bond breaking and dislocation processes at the crack tip [6]. While the influence of Al concentration on the yield stress and the dislocation mobility in NiAl has been extensively studied [7–9], including by atomistic simulations [10–14], no such detailed studies exist regarding the bond breaking processes leading to brittle cleavage.

Since typical bond coats have thicknesses of just up to 100 μm, testing their mechanical properties with standard methods is challenging. In-situ microscale mechanical testing of cantilevers milled by a focused ion beam (FIB) as introduced by Di Maio and Halford [15,16] can address these challenges and has been successfully applied to determine the properties of materials like Si [15], TiAl [16,17], W [18], Cu [19] and recently also of NiAl bond coats [20–22]. The study by Jaya et al. [20] was however conducted on polycrystalline parts of the bond coat so that grain boundary (GB) fracture dominated. The cantilevers in [21] were milled in individual grains, thus in principle allowing to compare their results to macroscopic fracture toughness on single crystalline NiAl, see e.g.,

* Corresponding author.
E-mail address: erik.bitzek@fau.de (E. Bitzek).

https://doi.org/10.1016/j.actamat.2022.117996

[23]. However, they only studied stoichiometric and $Ni_{60}Al_{40}$ coatings, which contained additional elements like Cr, Co and Pt.

A different approach to study the influence of Al concentration on the fracture behavior of NiAl thin films was used by Wellner et al. [24]. They used thermal cycling to induce strain in polycrystalline NiAl films of different homogeneous compositions on a Si substrate. Stoichiometric and Ni-rich NiAl films showed no cracks in their study, whereas Al-rich films exhibited pronounced cracking. However, the fracture toughness could only be determined for Al-rich films, where GB fracture dominated. A systematic study on the influence of off-stoichiometric composition on the fracture toughness of pure, single crystalline NiAl is currently lacking.

By performing microcantilever tests with different cantilever sizes and geometries on stoichiometric NiAl, Ast et al. could establish that the fracture toughness of NiAl at room temperature does not depend on the specimen size for characteristic lengths down to the micro scale [25]. In-situ microscale testing on compositionally graded single-crystalline NiAl thus present a unique model system to study the effect of off-stoichiometric composition on the fracture behavior of the intermetallic B2 $Ni_{0.5+/-x}Al_{0.5-/+x}$ phase.

A complementary approach to study the influence of Al concentration on the fracture toughness of NiAl is the use of atomistic simulations. Atomistic simulations have provided considerable insight in the atomic scale details of brittle fracture and crack tip plasticity in general [26]. Previous molecular static (MS) simulations of cracks in NiAl [27,28] have confirmed the experimental finding that the {110} planes are the primary and most probably the only natural cleavage planes of NiAl [23]. Dislocation emission was only observed for mixed mode loading or cracks on other planes. The emitted dislocations had ⟨100⟩ type Burgers vectors and were gliding on either {100} or {110} planes [27,28]. Molecular dynamics (MD) simulations at 5 K by Guo et al. [29] suggest that at low temperatures and high strains the stress-induced formation of martensite might contribute to the dissipation of strain energy ahead of the crack front. However, unphysical phase transitions at crack tips are a notorious problem for potentials of the embedded atom method (EAM) type [30,31]. All simulations so far were performed on stoichiometric NiAl. In general, very few simulations on the effect of the local chemical composition on crack-tip processes exist [26,32,33], and none of them in NiAl.

Here we combine nanomechanical tests on different regions of compositionally graded pure NiAl single crystals with atomistic simulations to investigate the influence of Al concentration on the fracture toughness of B2 NiAl.

2. Materials and methods

2.1. Sample preparation and testing

The influence of the chemical composition on the mechanical properties of the B2 phase was investigated using two single crystalline NiAl samples. Both were manufactured from pure elements with a purity of > 99.95% for Ni and > 99.999% for Al. Single crystals were cast by the Bridgman process and cooled with a cooling rate of 1K/min, see [34] for details of the sample preparation. According to [35,36] this slow cooling rate effectively reduces the number of thermal vacancies in the stoichiometric sample. To introduce a gradient in chemical composition, sample 1 was annealed in a furnace under air atmosphere at 1100 °C for 100 h The gradient, which developed due to the growth of alumina at the surface, was analyzed by energy dispersive X-ray spectroscopy. Sample 1 covers only the Ni-rich part of the phase field. Therefore, a second NiAl single crystal was aluminized in a pack cementation process and subsequently diffusion annealed to increase the Al-content (sample 2). The annealing temperatures to generate the

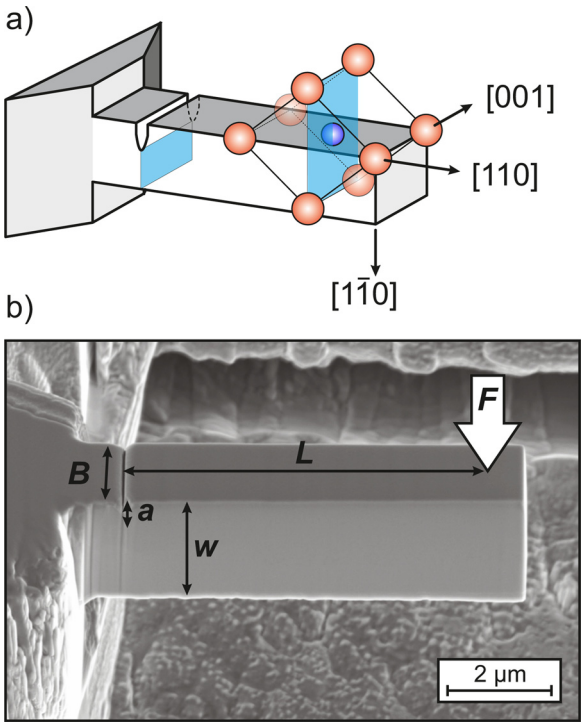

Fig. 1. a) Schematic of a microcantilever used to tests cracks in the "soft" orientation together with the NiAl unit cell and crystallographic directions. The crack plane is parallel to a (110) plane. b) SE micrograph of the geometry of a microcantilever.

Ni-rich and the Al-rich samples was 1100 °C at most and both samples were air-cooled afterwards.

The samples were subsequently ground with maximum orientation deviation of 5° and finished with electropolishing. The microcantilevers were then prepared according to the routine proposed by Iqbal et al. [17] along the edge of the sample in different positions of the chemical gradient. The advantage of this procedure is that all microcantilevers have the same crystallographic orientation, which was confirmed by electron backscattered diffraction (EBSD) measurements. The orientation of the microcantilevers is shown in Fig. 1a). Cracks with (110) plane orientation were introduced such that their crack front was oriented along the [001] direction. This orientation is often referred to as "soft" orientation, because the yield stress in tensile test along this direction is below 270 MPa [37,38], much lower than the one in the "hard" ⟨100⟩ direction (≈ 1400 MPa) [38]. The {110} planes were shown to be the natural cleavage planes of NiAl with a relatively low fracture toughness of 4 MPa $m^{1/2}$ [39]. The FIB milled microcantilevers were tested inside a scanning electron microscope (SEM) (Crossbeam 1540 EsB, Carl Zeiss AG, Germany) using a micromanipulator equipped with a force measurement system (FMS) (Kleindiek Nanotechnik, Germany). This allows the in-situ observation of the experiment and also to track the displacement with digital image correlation (DIC). Here, the software VEDDAC 5.1 [40] was used to evaluate the displacement fields. Fig. 1b) shows the final microcantilever geometry. In the following, the force that is applied by the indenter tip is denoted by F, the beam thickness by B, the width by W, the notch length by a and the distance from the indenter tip to the notch by L. Macroscopic experiments to determine the fracture toughness make use of nominally atomically sharp cracks introduced by fatigue pre-cracking. This is not possible in the microscopic setup. Instead, a notch is milled from the top with a fine FIB current of 10 pA and 30 kV acceleration voltage. The notch radius is approximately 10 nm, similar to the ones in [25]. For a

more detailed description of the testing methodology the reader is referred to [17,25,41].

2.2. Fracture mechanical analysis

The fracture toughness can be calculated from a notched bending test according to Eq. (1), if the plastic zone around the crack tip is small compared to the dimensions of the bending beam [42]:

$$K_{\mathrm{IQ}} = \frac{F_{\mathrm{Q}} L}{B W^{\frac{3}{2}}} f\left(\frac{a}{W}\right). \tag{1}$$

This equation uses the maximum force F_{max} for F_{Q} at the point of fracture and the beam geometry as introduced above. A geometry function for this beam geometry, which only depends on a and W was determined by finite element modeling (FEM) by Iqbal et al. [17].

According to the standards for fracture toughness determination [42,43], several requirements must be fulfilled. Due to the small size of the microcantilevers, not all of them could be met in this setup. The present approach was however shown to lead to results comparable to macroscopic tests [17,21,25]. If, however, the extent of the plastic zone at the crack tip is comparable to the specimen size, and the load-displacement curve shows a deviation from the elastic behavior, elastic-plastic fracture mechanics (EPFM) has to be used instead of Eq. (1). This requires the calculation of the J-integral that takes the elastic J_{el} and the plastic contribution J_{pl} into account [43]:

$$J = J_{\mathrm{el}} + J_{\mathrm{pl}} = \frac{K_{\mathrm{IQ}}^2 (1-\nu^2)}{E} + \frac{2A_{\mathrm{pl}}}{B(W-a)}. \tag{2}$$

Here K_{IQ} was calculated with Eq. (1) using $F_{\mathrm{Q}} = F_{0.95}$ and is then accordingly denoted by $K_{\mathrm{I},0.95}$. Following [43], $F_{0.95}$ was determined from the load-displacement plot as the force at the intersection of a straight line through the origin with a slope of $0.95E$ (see Fig. S1 in the supplementary material). The term $(1-\nu^2)/E$ in Eq. (2), which combines the Young's modulus E and Poisson ratio ν, was calculated from the elastic constants c_{ij} for the specific chemical composition [44] and the orientation of the crack following [45]. The plastic contribution J_{pl} was determined by using the area A_{pl} under the load-displacement curve, excluding the elastic contribution. The value of the constant was set to 2. The J-integral was then used with the expression

$$K_{\mathrm{Q},J} = \sqrt{\frac{JE}{1-\nu^2}} \tag{3}$$

to calculate the fracture toughness $K_{\mathrm{Q},J}$. As the samples did not fulfil all the requirements of the standards for fracture toughness determination, $K_{\mathrm{Q},J}$ is referred to as conditional fracture toughness [18].

2.3. Calculation of the theoretical fracture toughness

According to Griffith [46], the theoretical plane strain fracture toughness K_{G} can be expressed in terms of the energy release rate G by

$$K_{\mathrm{G}} = \sqrt{G_{\mathrm{G}} \tilde{E}^{-1}}, \tag{4}$$

with $\tilde{E}$ being an orientation dependent elastic constant that can be expressed in terms of c_{ij} [45]. For fracture to take place, the critical energy release rate G_{G} has to equal the energy of the surfaces $2\gamma_s$ created by the propagating crack:

$$G_{\mathrm{G}} = 2\gamma_s. \tag{5}$$

To evaluate K_{G} for different chemical compositions, c_{ij} and γ_s need to be determined for these compositions. This was achieved by performing MS calculations on a sample containing $15 \times 15 \times 15$ B2 NiAl unit cells. The respective off-stoichiometric compositions were modelled by randomly replacing Ni atoms by vacancies for Al-rich compositions, and Al atoms by Ni atoms on the Ni-rich side [47]. For the calculation, periodic boundary conditions (PBC) were used in all directions, and the box size was adjusted to obtain a stress-free minimum energy configuration. The surface energies were calculated by performing the MS simulations without PBC in the [110] direction. The calculations were performed on three different samples to provide an average value for the elastic constants and surface energies, independent of the individual atomic arrangement. All MS simulations were performed with the FIRE algorithm [48], and the EAM potential for NiAl by Pun and Mishin [49]. This potential was shown to reproduce well the equilibrium and defect properties of NiAl as determined from ab-initio simulations and experiments [49]. The relevant properties of this potential are provided in Table 1 in the supplementary material.

2.4. Atomistic fracture simulations

To study cracks under mode-I loading, an atomically sharp crack was introduced in a cylindrical sample of radius $R = 15$ nm by displacing the atoms according to the linear elastic solution of a crack in an infinite anisotropic elastic body [45,50]. PBCs were used in crack front ([001]) direction and atoms in a boundary layer of two times the cut-off radius of the potential were fixed. The setup is shown in Fig. S2 a) of the supplementary material. To determine the fracture toughness, MS calculations were performed where the applied stress intensity factor was iteratively increased in steps of $\Delta K_I = 0.007$ MPa $\mathrm{m}^{\frac{1}{2}}$. The critical stress intensity factor K_{Ic} was taken as the stress intensity at which the entire crack propagated by at least one atomic distance. For details of the simulation procedure see [30,51]. The calculations were performed on five samples to study the influence of the statistical distribution of atomic species in the off-stoichiometric samples. Doubling the sample size to $R = 30$ nm only lead at maximum to a change in the fracture toughness within one increment ΔK_I.

A different set-up (Fig. S2 b in the supplementary material) was used to study propagating cracks. A sample size of $70 \times 70 \times 20$ nm^3 with PBC in the [001] direction and fixed boundary conditions in the other directions was used. A blunted crack was introduced at the center of the sample by removal of one half-plane of atoms. Afterwards, the displacement field of a semi-elliptical crack was applied and the configuration was strained by a value slightly below the critical strain ε_G according to the Griffith energy balance as determined following [52]. The crack tip was located at 40% of the box length in $[\bar{1}10]$ direction. The entire configuration was relaxed ensuring zero stress in PBC direction. Standard MD simulations with a starting temperature of 0 K were performed while the sample is homogeneously strained in [110] direction at a strain rate of 10^8 s^{-1}, while maintaining zero stress in the orthogonal directions. Dislocations and their Burgers vectors were identified using slip vector analysis method [53]. The Open Visualization Tool (OVITO) was used for visualization of the atomistic simulation data [54].

3. Results

3.1. Microstructural and chemical analyses

The micrographs in backscattered electron contrast and the chemical composition of both B2 NiAl samples are shown in Fig. 2. With increasing Ni- and Al- content towards the right side of the samples a light grey and dark grey zone with the chemical gradient can be distinguished from the grey stoichiometric NiAl on the left side of both samples. The Al-content of sample 1 (Fig. 2a)

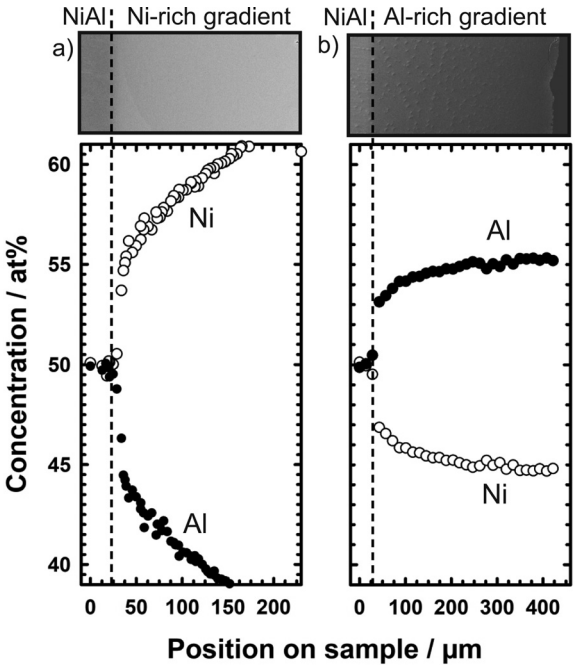

Fig. 2. a) SEM micrographs and corresponding concentration profiles of both samples with gradients towards high a) Ni- and b) Al-content.

decreases sharply within a distance of 10 μm from the stoichiometric composition to 45 at% and then gradually falls off to a concentration below 40 at%. The overall gradient in the chemical composition of sample 2 (Fig. 2b) is less steep than in sample 1, but also exhibits a jump in the concentration profile close to the stoichiometric composition. Since a martensitic phase transformation is know to occur during quenching from temperatures above 1000°C to room temperature [55,56], and for Ni-rich NiAl and NiAl-martensite also the formation of the orthorhombic Ni_5Al_3 phase has been reported for temperatures below 700°C [57], only measurements in the composition range between 40 and 55 at% Al were included in this study to guarantee that the fracture tests were performed in a single B2 phase.

3.2. In-situ microcantilever bending experiments

Depending on the composition, purely linear elastic as well as elastic-plastic load-displacement response of the notched microcantilevers were observed during the bending experiments. Figure S1 in the supplementary material shows two representative cases together with the constructions to determine the necessary parameters to calculate the fracture toughness according to Eq. (1) or (2). Representative load-displacement curves for different compositions can be found in Fig. 3a). The linear elastic parts do not have exactly the same slope, because the distance L of the crack from the loading point, i.e., the contact with the indenter, is not identical in all cases. The different L are however considered in the determination of the fracture toughness, Eqs. (1) and (3), see also Fig. 3b). The Al-rich microcantilevers show a linear-elastic behavior up to the point of fracture. Here, the maximum load F_{max} can be used for the value of F_Q in Eq. (1) to determine the fracture toughness. That way, the average fracture toughness of cantilevers with Al-rich compositions was determined to K_{Ic} of 2.1 ± 0.2 MPa $m^{1/2}$. Stoichiometric and Ni-rich NiAl microcantilevers, however, showed an elastic-plastic behavior. For these compositions, the condition $F_{max}/F_{0.95} > 1.1$ [43] is not met, and EPFM Eqs. (2) and (3) rather than LEFM (Eq. 1) has to be used.

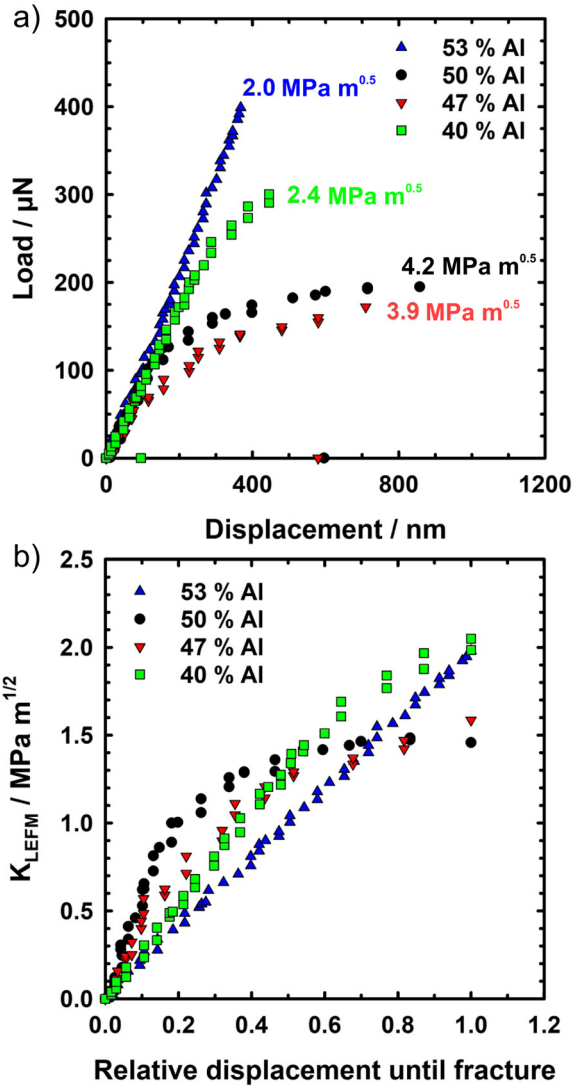

Fig. 3. (a) Representative experimental load-displacement curves for different Al-concentrations. (b) Plot of stress intensity factor vs. relative displacement as calculated from (a) using Eq. (1). The fracture toughness values determined by Eqs. (1) and (2) are provided next to the data points in (a).

Fig. 3a) clearly shows that for the Ni-rich compositions, A_{pl} decreased with decreasing Al-content. The fracture toughness values of all tested specimens are shown in Fig. 4. For purely brittle materials, Eqs. (1) and (3) lead to the same fracture toughness $K_{IQ} = K_{Q,J}$. Therefore, only $K_{Q,J}$ is plotted in Fig. 4. In the case fracture was accompanied by plastic deformation, the difference $K_{Q,J} - K_{IQ}$ were used to evaluate the amount of plasticity and the deviation from the purely elastic behavior of the load-displacement curve. The data points in Fig. 4 are color-coded according to this measure. In this Figure, the increase of plastic deformation and fracture toughness with increasing Al concentration in the Ni-rich part of the B2 phase is clearly evident. In Al rich NiAl, however, no plastic contribution to $K_{Q,J}$ could be discerned, and the fracture toughness appeared not to be influenced by the Al concentration. In the B2 part of sample 1, the microcantilever with composition closest to the stoichiometric composition had the highest fracture toughness ($K_{Q,J} = 4.8$ MPa $m^{1/2}$) and the largest deviation from the LEFM calculation ($K_{I,0.95} = 0.9$ MPa $m^{1/2}$).

Fracture surfaces of broken microcantilevers with different Al concentrations are shown in Fig. 5. Al-rich NiAl like the example at 53 at% in Fig. 5 shows typical cleavage fracture with a smooth

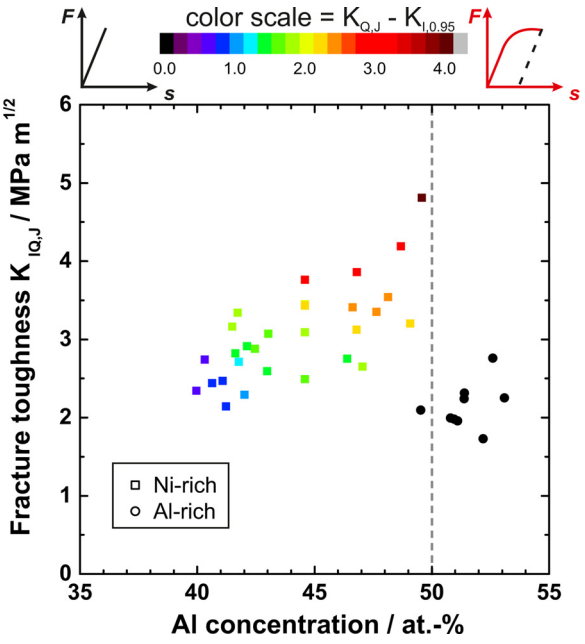

Fig. 4. Experimentally determined NiAl fracture toughness in dependence of Al concentration. The color code of the Ni-rich symbols (squares) represents the contribution of the plastic deformation to $K_{Q,J}$, as illustrated above the graph by the schematic load-displacement ($F-s$) curves for linear-elastic (left) fracture behavior of Al rich samples and elastic-plastic (right) fracture behavior of Ni rich concentrations.

crack onset right below the notch. Cracks in Ni-rich B2 NiAl, however, show a more ragged appearance, see Fig. 5. A common feature for all cracks in Ni-rich microcantilevers is a short initial phase of stable crack growth before final fracture. The arrow in Fig. 5 shows where the final fracture initiated. The step-like structure below and parallel to the notch suggests that the crack might have momentarily stopped before finally fracturing the cantilever. The initial stable crack growth can also be seen in movie M1 in the supplementary material.

3.3. Atomistic calculations

The lattice constant a_0, the elastic constants c_{ij} and the surface energy of (110) surfaces $\gamma_{(110)}$ were calculated for B2 NiAl for the composition range between 35 at% Al to 60 at% Al. Values for 45, 50, and 55 at% Al are provided in Table 1 of the supplementary material. While c_{11} is lowest for stoichiometric NiAl, c_{12} and c_{44} show a significant decrease with increased Al concentration. It is interesting to note that the Young's modulus in [110] direction $E_{[110]}$, however, shows an increase with increasing Al content, see Table 1 in the supplementary material. This can be understood by calculating the anisotropy ratio A, which also shows a decline with increasing Al concentration. With decreasing elastic anisotropy, the differences between the Young's moduli in different directions have to become smaller, i.e., $E_{[111]}$ decreases while $E_{[110]}$ and $E_{[100]}$ increase.

Based on the determined values of the surface energy and the elastic properties, the theoretical value for the critical stress intensity factor K_G was calculated following the Griffith concept [46] taking into account the anisotropic relationship between the applied K_I and the crack tip displacement field [45]. This theoretical fracture toughness according to LEFM assumes perfectly brittle fracture and is the lowest possible fracture toughness of this material. Its dependence on the composition is shown in Fig. 6. Its value is nearly constant in the Ni-rich part ($K_G \approx 0.76$ MPa $m^{1/2}$), slightly increases in the Al-rich part close to the stoichiometric composition and then decreases with increasing Al concentration.

The critical stress intensity factor K_{Ic} determined from the quasistatic fracture simulations are provided in Fig. 6 and Table 1. For the off-stoichiometric compositions, they are relatively close to K_G, while the stoichiometric composition figures a significantly larger K_{Ic} than K_G. This difference is commonly attributed to the lattice trapping [26,58] effect. Like in the study by Ludwig and Gumbsch [27], no dislocation emission was observed, also for the off-stoichiometric samples, see Fig. S3 in the supplementary material. The difference in their value for $K_{Ic} = 0.65$ MPa $m^{1/2}$ to our result of $K_{Ic} = 0.87$ MPa $m^{1/2}$ is most probably rooted in the different potential used in this study.

The generally large differences between atomistically and experimentally determined values of the fracture toughness which are obvious in Fig. 6 are well-known and are attributed to the idealized simulation setup, that precludes effects due to the activity of pre-existing dislocations, imperfect cleavage surfaces or atomic-scale crack tip blunting, which are all present under typical experimental conditions.

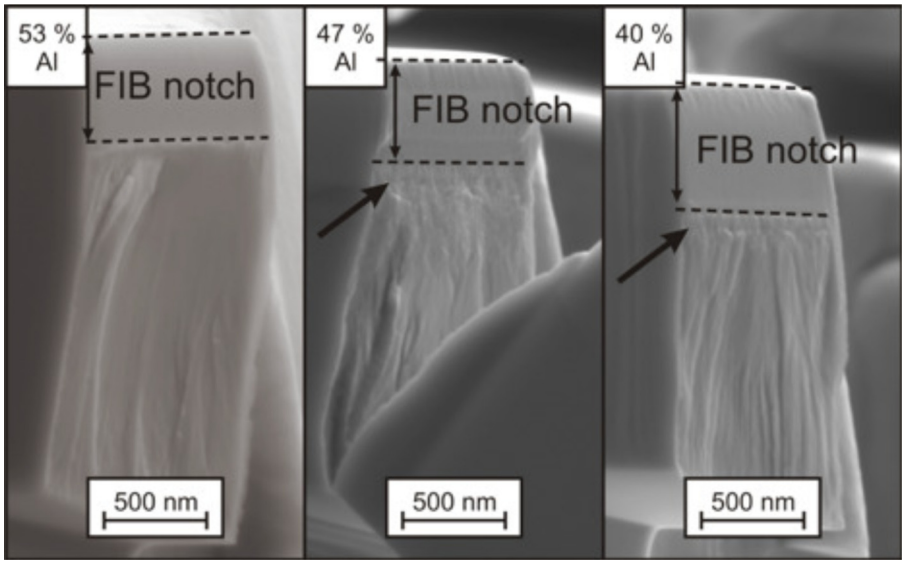

Fig. 5. Fracture surface of microcantilevers with different chemical composition given in at%. The arrows indicate where the initially stable crack growth changed to unstable crack propagation.

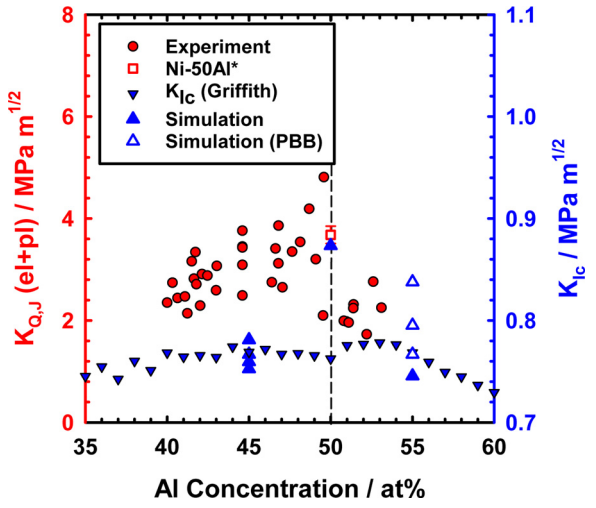

Fig. 6. Experimentally determined fracture toughness (identical to Fig. 4) together with the atomistically calculated fracture toughness following Griffith (Eq. 4) K_G and the results of the quasistatic simulations. Ni-50Al* represents the results from Ast et al. [25]. Please note the different scales for experimental data (red symbols, left axis) and atomistic calculations (blue symbols, right axis).

Table 1
Results of the quasistatic and dynamic fracture simulations: K_G – theoretical fracture toughness according to Eq. (4); K_{Ic} - critical applied stress intensity at which the crack either propagates or crack tip plasticity occurs; ε_G - critical strain according to the Griffith energy balance; ε_{cr} - critical strain at which large-scale bond breaking processes occur; ε_{dislo} – strain at which the first dislocation is emitted; Behavior: D – dislocation emission, B – brittle crack propagation.

	$Ni_{55}Al_{45}$	NiAl	$Ni_{45}Al_{55}$
Quasistatic:			
K_G (MPa $m^{1/2}$)	0.769	0.762	0.768
K_{Ic} (MPa $m^{1/2}$)	0.77 ±0.02	0.87	0.79±0.05
behavior:	B	B	B
Dynamic:			
ε_G (%)	2.4	2.6	2.1
ε_{cr} (%)	3.22	3.32	2.21
ε_{dislo} (%)	4.1	4.0	3.4
behavior:	B+D	B+D	B+D

Whereas the determination of K_{Ic} by static simulations and the concept of lattice trapping are well-established for uniform or ordered structures [59], determining the fracture toughness for crystals with atomic-scale disorder like in the off-stoichiometric cases is less straight-forward. In general, a crack can propagate by breaking all crack-tip bonds within one load increment, or by subsequently breaking of individual or multiple bonds during successive load increments.

The first case is exemplary shown in Fig. 7b for the case for stoichiometric NiAl, where all crack-tip bonds are identical and a large lattice trapping was observed. Similarly, all cracks in Ni-rich NiAl propagated within one load increment, see, e.g., Fig. 7a. However, the locally varying bonding situation at the crack tip resulted to negligible lattice trapping, see Table 1.

In contrast all but one crack in Ni-55 at%Al showed prior bond breaking (PBB) processes before the crack propagated at K_{Ic}, see Figs. 7c and 8. Interestingly, PBB in the Al-rich samples was only observed when the vacancies were not located directly at the crack front and these samples also showed higher fracture toughness values than the sample with vacancies directly at the crack tip that showed no PBB. A possible explanation could be that the strength of metallic bonds as modelled by the EAM formalism depends on the environment, with lower coordinated atoms having stronger individual bonds [60]. In this context it is important to point out that it was recently found that EAM potentials have one order of magnitude higher lattice trapping than what would be expected from Density Functional Theory calculations [61]. However, prior breaking or reorganization of some crack-tip bonds before the entire crack propagates can still be expected for cracks in disordered media.

It is furthermore interesting to note that in Fig. 6 K_{Ic} could be smaller than predicted by the Griffith equation. This can be explained by the fact that the propagating crack produces only a surface increment of one atomic spacing, whereas the surface energy used to calculate K_{Ic} according to Griffith in Fig. 6 was averaged over a large area as well as multiple realizations. Crack advance for values of K_{Ic} smaller than the thermodynamically averaged K_G is thus possible in the small setups used in typical atomistic simulations. The present, established method therefore can not be used to determine thermodynamically reasonable values for the fracture toughness in atomically disordered systems. This would require the propagation of the crack over large distances, which – under pure K-controlled loading – is not possible with the currently available boundary conditions.

Crack propagation therefore was studied using a strain- rather than a K-controlled setup. Snapshots from the MD simulations are shown in Fig. 9. For the stoichiometric sample, Fig. 9b), the crack propagated for a couple of lattice constants and then started to emit a dislocation on the [100](010) slip system. The crack was slowed down by the emission of the dislocation, but under the constant strain rate of 10^8 s^{-1}, the crack propagated further and emitted another dislocation on the mirror symmetric $[0\bar{1}0](100)$ slip system. The entire process can be seen in supplementary movie M2.

The sample with 45 at% Al, Fig. 9a), behaved similarly to the stoichiometric sample: The Griffith strain ε_G at which the elastically stored energy in the sample is identical to the surface energy as well as the critical strain ε_{cr} at which the crack started to propagate were comparable. Also the emission of the first dislocation (on the $[0\bar{1}0](100)$ system) took place at roughly the same strain, see also Table 1. The emission of the second dislocation, however, took place significantly later compared to the stoichiometric sample, see supplementary movie M3.

The Griffith strain for the sample with 55 at% Al, Fig. 9c), was smaller than for the other samples (Table 1). More importantly, however, is that crack propagation started at a value of ε_{cr} that was only slightly larger than ε_G and 50% lower compared to the stoichiometric and Ni-rich samples. In addition, the crack front appeared rougher and dislocation emission started on both slip systems, see also supplementary movie M4. The crack propagation distance as a function of time for all the compositions is shown in Table 2 in the supplementary material.

Large slip traces that are in agreement with the observed $\langle 100 \rangle \{010\}$ dislocations were also seen in microcantilever tests performed in the same orientation [25]. That dislocations were observed in the dynamic but not in the static simulations can have multiple reasons. The large strains necessary in the clamped strip geometry could have lowered the energy barrier to nucleate dislocations through the well-known tension-shear coupling [62]. Dislocation emission could also be related to a dynamic crack tip instability, or the kinks and jogs in the propagating crack front provided preferable sites for dislocation nucleation [63]. In general it has been shown, that the emission of loops rather than straight dislocation lines as enforced by the boundary conditions and the static minimization in the K-controlled setup, Fig. S2a) in the supplementary material, requires lower activation energy [64].

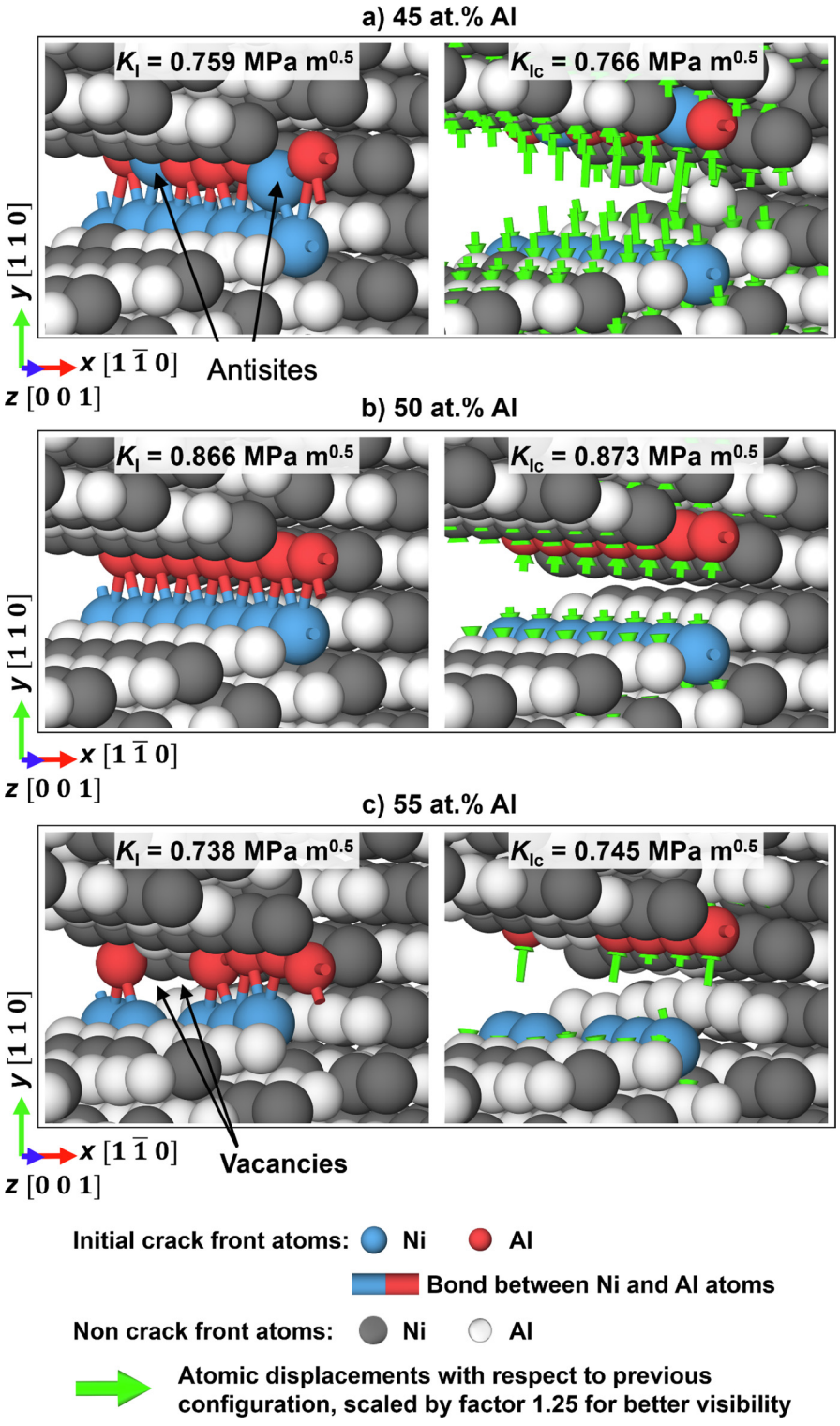

Fig. 7. Example for the determination of the critical stress intensity factor (K_{Ic}). In all cases the entire crack propagated by one atomic distance within one load increment, resulting in a unique value for K_{Ic}.

4. Discussion

The fracture toughness of stoichiometric B2 NiAl has been determined by macroscopic fracture experiments to lie between 5 and 9 MPa m$^{1/2}$ [23,34,39]. Using the same methodology as in this paper, Ast et al. showed that these values were reproduced in microscale experiments [25], and their values agree well with the presented results on near-stoichiometric, Ni-rich NiAl, see Fig. 6.

While the experiments on the Ni-rich samples showed a continuous decrease of fracture toughness and accompanying plastic deformation (Fig. 4), the Al-rich samples showed nearly constant low fracture toughness values between 1.7 and 2.4 MPa m$^{1/2}$, even for minute deviations from the stoichiometric composition.

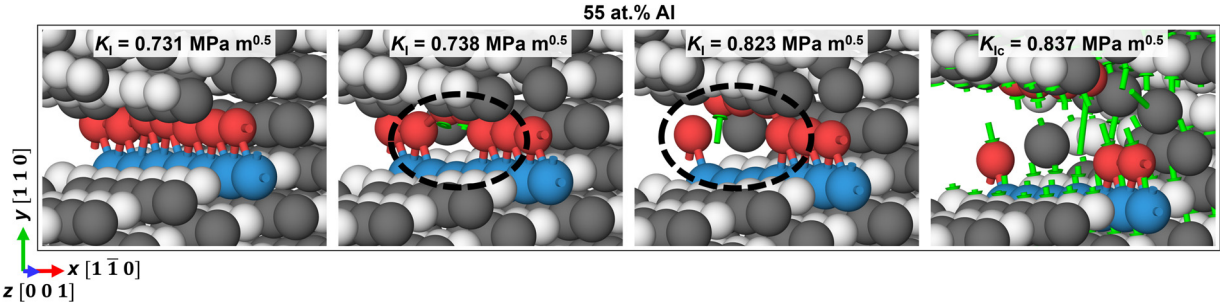

Fig. 8. Example for the determination of the critical stress intensity factor when prior bond breaking (PBB) processes take place before the entire crack has advanced by one atomic distance at the load K_{Ic}. This behavior was only observed when structural vacancies were present close to the crack tips in Ni- 55 at.%Al. PBB are highlighted by dashed ellipses. The atom colours and green arrows have same meaning as in figure 7.

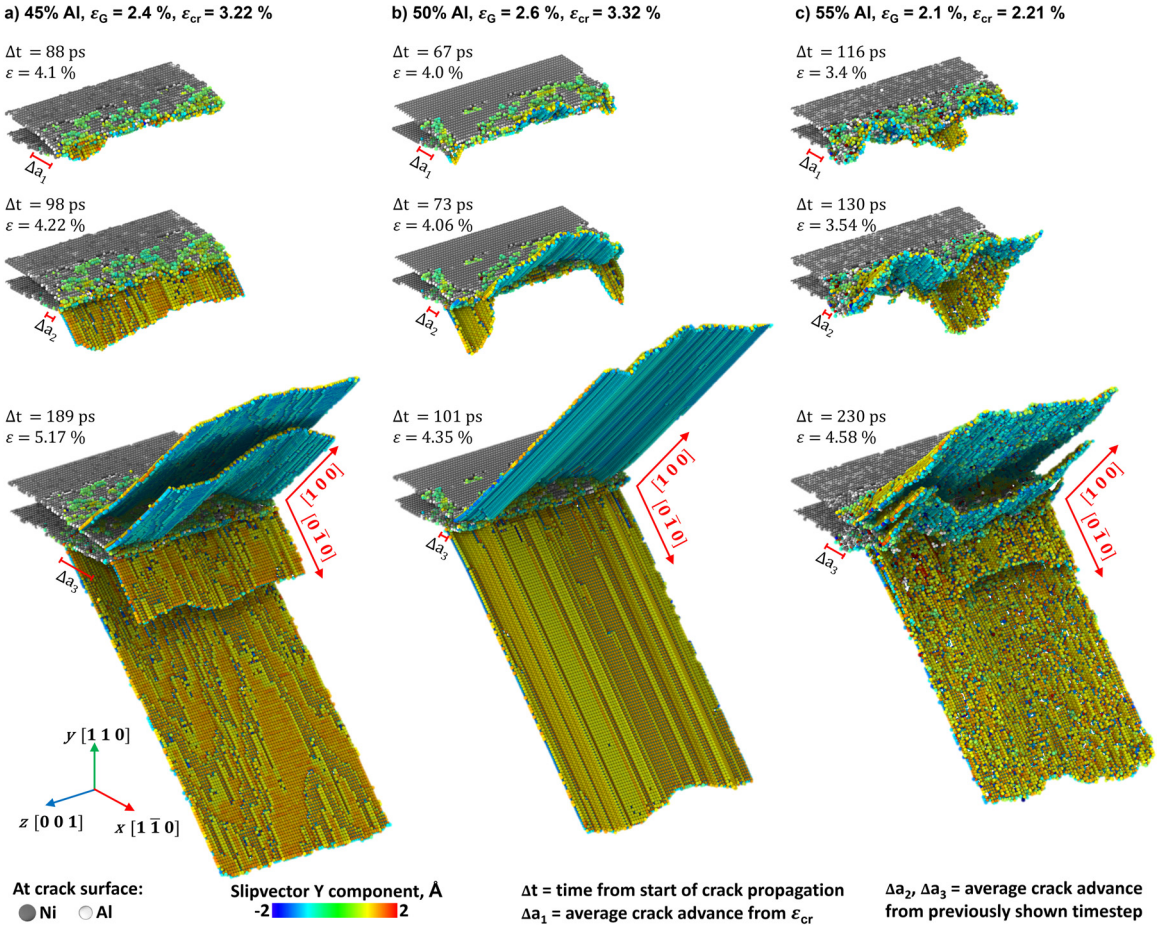

Fig. 9. Snapshots from the MD simulations of cracks in NiAl samples of different compositions subjected to a constant strain rate $\varepsilon_{yy} = 10^8$ s^{-1}: during the process of dislocation emission (top row), propagation of crack and dislocations (middle row), and emission of further dislocations (bottom row). Only atoms belonging to defects other than the initial crack (dark grey: Ni, light gray: Al) are shown using slip vector analysis. The arrows shown next to the dislocations in the bottom row indicate the Burgers vector directions of the dislocations.

This compares well with the Al concentration-independent fracture toughness values of 2.2-2.9 MPa m$^{1/2}$ determined by Wellner et al. [24] for polycrystalline NiAl films with 50.4-52.4 at.% Al. An increase in Al concentration therefore seems to affect the fracture toughness of NiAl in a qualitatively different way than an increase in Ni concentration.

Fracture toughness is traditionally seen as being inversely proportional to the tensile strength of the material, as a higher yield stress σ_y implies a smaller plastic zone and less dissipation of elastic strain energy as well as less efficient shielding of the crack tip by the motion and multiplication of dislocations. In contrast to its impact on fracture toughness, the effect of off-stoichiometric composition on the hardness of NiAl has been well studied. Figure 10a) shows the microhardness determined by Pike et al. [8] as function of the deviation Δc from the stoichiometric composition. The hardness increases continuously with increasing deviation from the stoichiometric composition, which is mainly caused by constitutional defects such as anti-site Ni atoms or vacancies on Ni sites. Thermal defects in NiAl and therefore the thermal history can have a noticeable influence on the hardness of stoichiometric NiAl, too. However, in our samples, we do not expect a significant influence of thermal defects on the fracture toughness of our stoichiometric as well as off-stoichiometric Ni- and Al-rich samples. The stoichiometric samples were cooled with a very slow cooling

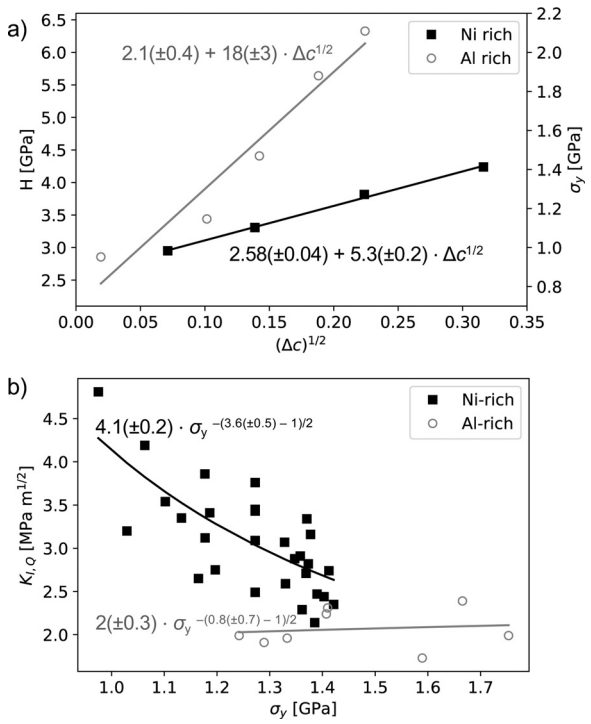

Fig. 10. a) Hardness H and yield stress $\sigma_y = H/3$ of off-stoichiometric NiAl as determined by Pike et al. [8] shown as function of the square root of the deviation from the stoichiometric concentration Δc for Al- and Ni-rich compositions. The results of linear fits are provided next to the plots of the fit function. b) Fracture toughness values from Fig. 4 as function of σ_y as calculated from the fits in a). The lines indicate fits of the RKR model for the yield-stress dependence of the fracture toughness with the shown parameters.

rate of 1K/min after casting, which reduces the number of thermal defects significantly. Similarly, the temperatures of the annealing procedure or the pack cementation process to generate the off-stoichiometric samples did not exceed 1100°C and the subsequent cooling rate was also rather slow. Thermal vacancies, and thus also tripple defects consisting of two thermal vacancies on the Ni sublattice pairing with the anti-site Ni, are therefore not expected to play a major role influencing the fracture toughness of our samples. Furthermore, the effect of thermal defects on the mechanical properties has been shown to be generally of minor importance for off-stoichiometric compositions [8].

As shown by Schroll and Gumbsch [13], the binding energy of the point defects associated with the deviation from the stoichiometric composition to dislocations decreases very quickly with the distance from the dislocation core. Therefore Fleischer's theory instead of the Labusch theory of solid solution strengthening [65] has to be applied as shown by the proportionality of the hardness H to $\sqrt{\Delta c}$ [8]. This proportionality enables us to map the concentrations in Fig. 4 onto values for $\sigma_y = H/3$ using the fits shown in Fig. 10a). The resulting correlation between fracture toughness and yield stress is shown in Fig. 10b).

According to the classic model by Ritchie, Knott and Rice (RKR)[66] the fracture toughness K_{Ic} is proportional to [67]

$$K_{Ic} \propto \sigma_y^{-(N-1)/2}, \tag{6}$$

assuming a Ramberg-Osgood relationship $\varepsilon/\varepsilon_y = \sigma/\sigma_y + \alpha(\sigma/\sigma_y)^N$ between stress σ and strain ε, with the subscript y indicating the value at yielding, α a constant and N the work hardening exponent. The corresponding fits in Fig. 10b) show that the fracture toughness in the Ni-rich regime follows this model, with a work hardening exponent $N = 3.6 \pm 0.5$ that agrees well with the value $N = 3$ determined by Bowman et al. [68] for stoichiometric NiAl with a grain size of 10 μm. Al-rich NiAl, however, does not follow the RKR relationship, with the fit requiring an unphysical value of $N < 1$. The composition dependence of the obtained fracture toughness values is thus consistent with the generally recognized composition dependence of hardness for Ni-rich NiAl, but this is *not* the case for Al-rich NiAl.

Clearly, the fact that structural vacancies on the Al-rich side are more potent hardeners than Ni-antisites in the Ni-rich regime can by itself not explain the different dependence of the fracture toughness on the off-stoichiometric concentration. Even for similar values of σ_y the fracture toughness can be significantly different, see Fig. 10b). Similarly, the degree of plasticity (Fig. 4) and the fracture surfaces (Fig. 3) are significantly different for Ni- and Al-rich specimens with identical Δc.

The atomistic calculations show that these differences can not be explained by differences in the theoretical fracture toughness K_G (Fig. 6) or in the statically determined fracture toughness (Table 1). Also the MD simulations show the same type and number of dislocations being emitted in the same order for $Ni_{55}Al_{45}$ and $Ni_{45}Al_{55}$ (Fig. 9).

However, the MD simulations show that the additional strain $\varepsilon_{cr} - \varepsilon_G$ necessary to initiate crack propagation from a crack loaded at the theoretical fracture strain ε_G is significantly lower in the Al-rich sample than both the Ni-rich and the stoichiometric sample (Table 1). Crack propagation therefore seems to be favored by the presence of structural vacancies. A detailed analysis of the stoichiometric sample with high time resolution shows that even at 0 K the crack propagated by the nucleation and migration of kink pairs, see Fig. 11. The same mechanism was observed in off-stoichiometric compositions and is shown in supplementary material Fig. S2. Similar crack propagation by kinks was also recently observed in Si [69]. It is important to note, that this dynamical process can not be captured by the typical static simulations.

The intersection of the crack front with structural vacancies automatically leads to kinks on the crack front. The dynamics of brittle crack propagation will therefore in Al-rich samples be dominated by the propagation of the kinks rather than their nucleation.

Although no triple defects were explicitly included in the simulations, the presence of two vacancies in the triple defect should have the same effect of producing kinks on the crack front than single vacancies.

Structural vacancies thereby play a dual role in fracture of Al-rich NiAl: they not only impede dislocation motion and thereby reduce plastic dissipation and shielding, but additionally facilitate crack propagation, by lowering the kinetic barrier for crack advance. The same mechanisms and behavior should therefore also be observable in other B2 aluminides in which structural vacancies occur, like FeAl and CoAl. Furthermore, the B2 phase in NiAl in-situ composites, which have been suggested as novel high temperature alloy system [70], might experience a similar embrittlement by structural vacancies.

5. Summary

Microbending tests on notched cantilever beams were used to study cracks propagating on {101} planes in ⟨110⟩ direction in stoichiometric and off-stoichiometric B2 NiAl single crystals. While stoichiometric NiAl showed the highest fracture toughness, the fracture toughness and plastic energy dissipation decreased gradually with increasing Ni-concentration, Al-rich NiAl showed a concentration-independent low fracture toughness and no signs of accompanying plasticity. While the dependence of the fracture toughness on the yield stress of Ni-rich NiAl can be successfully described by the RKR model, no such correlation exists for the Al-rich samples.

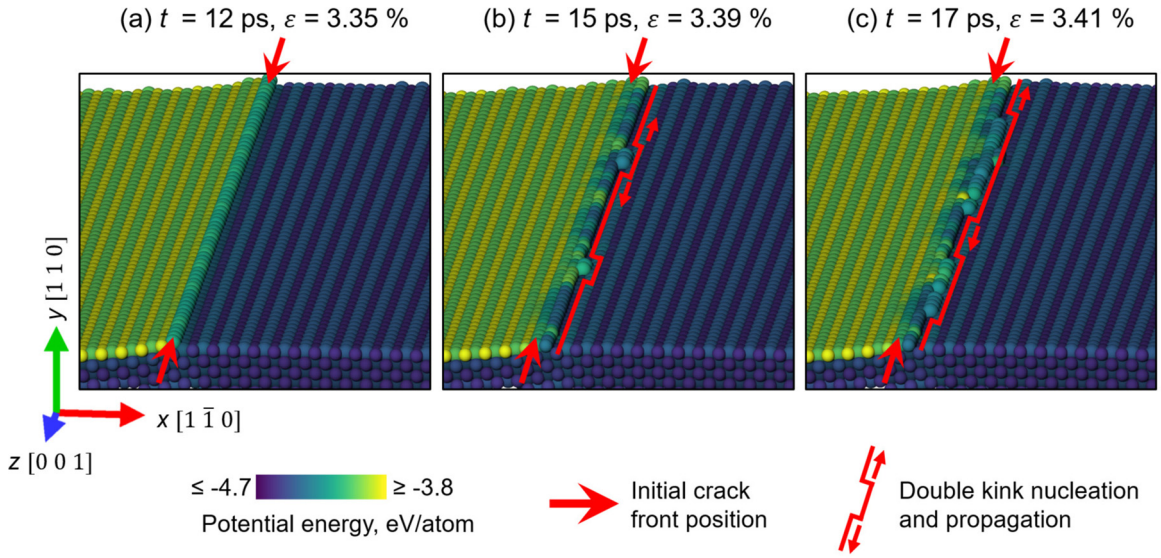

Fig. 11. Crack propagation by the nucleation and migration of kink pairs in the stoichiometric sample. Crack propagates along *x* direction. Only the lower half of the sample is shown with atoms colored by their potential energy, clearly showing the fracture surface. (a) Initial crack front position, (b) kink pair nucleation, (c) kink pair migration.

Atomistic calculations showed that the theoretical fracture toughness as well as the fracture toughness determined from static simulations were comparable for Ni- and Al-rich NiAl. Similarly, MD simulations showed no significant difference in crack tip plasticity in both regimes.

Detailed analysis of the MD simulations revealed that crack propagation took place by the nucleation and propagation of kink-pairs. As the intersection of the crack front with vacancies automatically generates kink-pairs, structural vacancies can – in addition to their role as potent obstacles for dislocations – act as crack front kink pairs.

Thus rather than affecting the theoretical fracture toughness according to the thermodynamic Griffith criterion, structural vacancies in Al-rich NiAl lower the kinetic barrier for crack propagation, explaining the observed different concentration dependence of the fracture toughness. Similar observations are also expected for fracture in other off-stoichiometric B2 aluminides and their composites.

In addition, the static, *K*-controlled simulations showed that the usual approach for determining the fracture toughness, namely identifying the onset of crack propagation and the use of relatively short crack front segments, can not be applied to fracture in atomically disordered systems. Here, the development of new statistical approaches is required.

Declaration of Competing Interest

The authors declare that they have no known competing financial interests or personal relationships that could have appeared to influence the work reported in this paper.

Acknowledgements

SK, PNB, and EB acknowledge F. Houllé and A. Atila for their help in preparing figures and movies. The authors wish to acknowledge funding from the German Research Foundation (DFG) through the graduate schools 1229 and 1896 and project C3 of the SFB/Transregio 103 (Single Crystal Superalloys). PNB, SK and EB acknowledge funding from the European Research Council (ERC) under the European Union's Horizon 2020 research and innovation programme (grant agreement No 725483).

Supplementary material

Supplementary material associated with this article can be found, in the online version, at doi:10.1016/j.actamat.2022.117996.

References

[1] R. Darolia, NiAl alloys for high-temperature structural applications, JOM J. Miner. Met. Mater. Soc. 43 (3) (1991) 44–49.
[2] D.B. Miracle, Overview No. 104 The physical and mechanical properties of NiAl, Acta Metall. Mater. 41 (3) (1993) 649–684.
[3] R. Darolia, Ductility and fracture toughness issues related to implementation of NiAl for gas turbine applications, Intermetallics 8 (9-11) (2000) 1321–1327.
[4] G.W. Goward, Progress in coatings for gas turbine airfoils, Surf. Coatings Technol. 108-109 (0) (1998) 73–79.
[5] M. Arana Antelo, P. Johnson, K. Ostolaza, J. Bressers, Analysis of the fracture behaviour of an aluminide coating on a single-crystal superalloy under tensile conditions, Mater. Sci. Eng. A 247 (1998) 40–50.
[6] P. Gumbsch, Modelling brittle and semi-brittle fracture processes, Mat. Sci. Eng. A 319-321 (2001) 1–7.
[7] I. Baker, A review of the mechanical properties of B2 compounds, Mater. Sci. Eng. A 192/193 (1995) 1–13.
[8] L.M.A. Pike, Y.A.A. Chang, C.T.B. Liu, Point defect concentrations and hardening in binary B2 intermetallics, Acta Mater. 45 (9) (1997) 3709–3719.
[9] L.M. Pike, I.M. Anderson, C.T. Liu, Y.A. Chang, Site occupancies, point defect concentrations, and solid solution hardening in B2 (Ni,Fe)Al, Acta Mater. 50 (15) (2002) 3859–3879.
[10] R. Schroll, P. Gumbsch, V. Vitek, On the structure and mobility of dislocations in NiAl, Mater. Sci. Eng. a-Struct. Mater. Prop. Microstruct. Process. 233 (1-2) (1997) 116–120.
[11] P. Gumbsch, R. Schroll, Atomistic aspects of the deformation of NiAl, Intermetallics 7 (3-4) (1999) 447–454.
[12] R. Schroll, V. Vitek, P. Gumbsch, Core properties and motion of dislocations in NiAl, Acta Mater. 46 (3) (1998) 903–918.
[13] R. Schroll, P. Gumbsch, Atomistic study of the interaction between dislocations and structural point defects in NiAl, Phys. Status Solidi A 166 (1998) 475–488.
[14] N.I. Medvedeva, Y.N. Gornostyrev, D.L. Novikov, O.N. Mryasov, A.J. Freeman, Ternary site preference energies, size misfits and solid solution hardening in NiAl and FeAl, Acta Mater. 46 (10) (1998) 3433–3442.
[15] D. Di Maio, S.G. Roberts, Measuring fracture toughness of coatings using focused-ion-beam-machined microbeams, J. Mater. Res. 20 (2) (2005) 299–302.
[16] T.P. Halford, K. Takashima, Y. Higo, P. Bowen, Fracture tests of microsized TiAl specimens, Fatigue Fract. Eng. Mater. Struct. 28 (8) (2005) 695–701.
[17] F. Iqbal, J. Ast, M. Göken, K. Durst, In situ micro-cantilever tests to study fracture properties of NiAl single crystals, Acta Mater. 60 (3) (2012) 1193–1200.
[18] S. Wurster, C. Motz, R. Pippan, Characterization of the fracture toughness of micro-sized tungsten single crystal notched specimens, Philos. Mag. 92 (February 2012) (2012) 1803–1825.
[19] E. Demir, F. Roters, D. Raabe, Bending of single crystal microcantilever beams of cube orientation: finite element model and experiments, J. Mech. Phys. Solids 58 (10) (2010) 1599–1612.

[20] B.N. Jaya, V. Jayaram, S.K. Biswas, A new method for fracture toughness determination of graded (Pt,Ni)Al bond coats by microbeam bend tests, Philos. Mag. 92 (25–27) (2012) 3326–3345.
[21] R. Webler, M. Krottenthaler, S. Neumeier, K. Durst, M. Göken, Local fracture toughness and residual stress measurements on nial bond coats by micro cantilever and FIB based bar milling tests, John Wiley & Sons, Inc., 2012, pp. 93–102.
[22] B.N. Jaya, V. Jayaram, Crack stability in edge-notched clamped beam specimens: modeling and experiments, Int. J. Fract. 188 (2) (2014) 213–228.
[23] K.-M. Chang, R. Darolia, H.A. Lipsitt, Cleavage fracture in B2 aluminides, Acta Metall. Mater. 40 (10) (1992) 2727–2737.
[24] P. Wellner, O. Kraft, G. Dehm, J. Andersons, E. Arzt, Channel cracking of beta–NiAl thin films on Si substrates, Acta Mater. 52 (8) (2004) 2325–2336.
[25] J. Ast, T. Przybilla, V. Maier, K. Durst, M. Göken, Microcantilever bending experiments in NiAl - Evaluation, size effects, and crack tip plasticity, J. Mater. Res. 29 (18) (2014) 2129–2140.
[26] E. Bitzek, J.R. Kermode, P. Gumbsch, Atomistic aspects of fracture, Int. J. Fract. 191 (1-2) (2015) 13–30.
[27] M. Ludwig, P. Gumbsch, Cleavage fracture and crack tip dislocation emission in B2 NiAl: an atomistic study, Acta Mater. 46 (9) (1998) 3135–3143.
[28] D. Farkas, Bulk and intergranular fracture behaviour of NiAl, Philos. Mag. A 80 (6) (2000) 1425–1444.
[29] Y.F. Guo, Y.S. Wang, W.P. Wu, D.L. Zhao, Atomistic simulation of martensitic phase transformation at the crack tip in B2 NiAl, Acta Mater. 55 (11) (2007) 3891–3897.
[30] J.J. Möller, E. Bitzek, Comparative study of embedded atom potentials for atomistic simulations of fracture in alpha-iron, Model. Simul. Mater. Sci. Eng. 22 (4) (2014) 45002.
[31] J.J. Möller, M. Mrovec, I. Bleskov, J. Neugebauer, T. Hammerschmidt, R. Drautz, C. Elsässer, T. Hickel, E. Bitzek, {110} planar faults in strained bcc metals: origins and implications of a commonly observed artifact of classical potentials, Phys. Rev. Mater. 2 (9) (2018) 093606.
[32] J. Kermode, L. Ben-Bashat, F. Atrash, J. Cilliers, D. Sherman, A. De Vita, Macroscopic scattering of cracks initiated at single impurity atoms, Nat. Commun. 4 (2013) 2441.
[33] S.L. Liu, C.Y. Wang, T. Yu, Effect of Re and W upon brittle fracture in Ni3Al cracks by atomic simulation, Comput. Mater. Sci. 110 (2015) (2015) 261–269.
[34] G. Bergmann, H. Vehoff, Precracking of NiAl single crystals by compression–compression fatigue and its application to fracture toughness testing, Scr. Met. Mater. 30 (8) (1994) 969–974.
[35] P. Nagpal, I. Baker, Effect of cooling rate on hardness of FeAl and NiAl, Metall. Trans. A 21 (8) (1990) 2281–2282, doi:10.1007/BF02647891.
[36] J.M. Brzeski, J.E. Hack, R. Darolia, R.D. Field, Strain aging embrittlement of the ordered intermetallic compound NiAl, Mater. Sci. Eng. A 170 (1-2) (1993) 11–18, doi:10.1016/0921-5093(93)90364-K.
[37] F. Ebrahimi, S. Shrivastava, Brittle-to-ductile transition in NiAl single crystal, Acta Mater. 46 (1998) 1493–1502.
[38] R.T. Pascoe, C.W.A. Newey, The mechanical behaviour of the intermediate phase NiAl, Met. Sci. 2 (1) (1968) 138–143.
[39] F. Thome, M. Göken, H. Vehoff, Study of the fracture behavior in soft and hard oriented NiAl single crystals by AFM, Intermetallics 7 (3-4) (1999) 491–499.
[40] Digital Image Correlation VEDDAC 5.1-User's Manual, Chemnitzer Werkstoffmechanik GmbH, Chemnitz, Germany, 2011.
[41] J. Schaufler, C. Schmid, K. Durst, M. Göken, Determination of the interfacial strength and fracture toughness of a-C:H coatings by in-situ microcantilever bending, Thin Solid Films 522 (2012) (2012) 480–484.
[42] A. International, ASTM Standard E399, Standard Test Method for Plane-Strain Fracture Toughness of Metallic Materials, Technical Report, ASTM International, West Conshohocken, PA, United States, 1997.
[43] A. International, ASTM Standard E1820, Standard Test Method for Measurement of Fracture Toughness, Technical Report, ASTM International, West Conshohocken, PA, United States, 2013.
[44] N. Rusovic, H. Warlimont, Elastic behaviour of β_2-NiAl alloys, Phys. Status Solidi Appl. Res. 44 (2) (1977) 609–619.
[45] G.C. Sih, H. Liebowitz, Fracture, An Advanced Treatise, Academic, 1968, pp. 67–190.
[46] A.A. Griffith, The Phenomena of Rupture and Flow in Solids, Phil. Trans. Roy. Soc. London A 221 (582-593) (1921) 163–198.
[47] B. Meyer, G. Bester, M. Fähnle, Structural vacancies in B2 CoAl and NiAl, Scr. Mater. 44 (10) (2001) 2485–2488.
[48] J. Guénolé, W.G. Nöhring, A. Vaid, F. Houllé, Z. Xie, A. Prakash, E. Bitzek, Assessment and optimization of the fast inertial relaxation engine (FIRE) for energy minimization in atomistic simulations and its implementation in LAMMPS, Comput. Mater. Sci. 175 (2020) 109584.
[49] G.P.P. Pun, Y. Mishin, Development of an interatomic potential for the Ni-Al system, Phil. Mag. 89 (34-36) (2009) 3245–3267.
[50] J.J. Möller, A. Prakash, E. Bitzek, FE2AT–finite element informed atomistic simulations, Model. Simul. Mater. Sci. Eng. 21 (5) (2013) 055011.
[51] J.J. Möller, E. Bitzek, Fracture toughness and bond trapping of grain boundary cracks, Acta Mater. 73 (2014) 1–11.
[52] E. Bitzek, P. Gumbsch, Mechanisms of Dislocation Multiplication at Crack Tips, Acta Mater. 61 (4) (2013) 1394–1403.
[53] J.A. Zimmerman, C.L. Kelchner, P.A. Klein, J.C. Hamilton, S.M. Foiles, Surface step effects on nanoindentation, Phys. Rev. Lett. 87 (2001) 165507.
[54] A. Stukowski, Visualization and analysis of atomistic simulation data with OVITO–the open visualization tool, Modell. Simul. Mater. Sci. Eng. 18 (1) (2009) 015012.
[55] J. Smialek, Martensite in NiAl oxidation-resistant coatings, Metall. Trans. 2 (1973) 913–915.
[56] J. Smialek, R. Hehemann, Transformation temperatures of martensite in beta-phase nickel aluminide, Metall. Trans. 4 (1973) 1571–1575.
[57] T. Cheng, Ni5Al3 phase in heat cycled Nickel-rich NiAl, J. Mater. Sci. Lett. 15 (1999) 285–289.
[58] R. Thomson, C. Hsieh, V. Rana, Lattice Trapping of Fracture Cracks, J. Appl. Phys. 42 (1971) 3154–3160.
[59] P. Andric, W.A. Curtin, Atomistic modeling of fracture, Modell. Simul. Mater. Sci. Eng. 27 (1) (2019).
[60] D.G. Pettifor, Bonding and Structure of Molecules and Solids, Clarendon Press, 1995.
[61] P. Hiremath, S. Melin, E. Bitzek, P.A. Olsson, Effects of interatomic potential on fracture behaviour in single- and bicrystalline tungsten, Comput. Mater. Sci. 207 (2022) 111283, doi:10.1016/j.commatsci.2022.111283.
[62] Y.M. Sun, G.E. Beltz, J.R. Rice, Estimates from atomic models of tension shear coupling in dislocation nucleation from a crack-tip, 1993, pp. 67–85.
[63] P.A. Gordon, T. Neeraj, M.J. Luton, The effect of heterogeneities on dislocation nucleation barriers from cracktips in α-Fe, Model. Simul. Mater. Sci. Eng. 17 (2) (2009) 25005.
[64] T. Zhu, J. Li, S. Yip, Atomistic study of dislocation loop emission from a crack tip, Phys. Rev. Lett. 93 (2) (2004) 25503.
[65] A. Argon, Strengthening mechanisms in crystal plasticity, Oxford University Press, 2008.
[66] R. Ritchie, J.F. Knott, J.R. Rice, On the relationship between critical tensile stress and fracture toughness in mild steel by, J. Mech. Phys. Solids 21 (1973) 395–410.
[67] D.A. Curry, Grain-size dependence of cleavage fracture toughness in mild steel, Nature 276 (1978) 50–51.
[68] R.R. Bowman, R.D. Noebe, S.V. Raj, I.E. Locci, Correlation of deformation mechanisms with the tensile and compressive behavior of NiAl and NiAl(Zr) intermetallic alloys, Metall. Trans. A 23 (5) (1992) 1493–1508.
[69] J.R. Kermode, A. Gleizer, G. Kovel, L. Pastewka, G. Csányi, D. Sherman, A.D. Vita, Low speed crack propagation via kink formation and advance on the silicon (110) cleavage plane, Phys. Rev. Lett. 115 (2015) 135501.
[70] C. Gombola, A. Kauffmann, G. Geramifard, M. Blankenburg, M. Heilmaier, Microstructural investigations of novel high temperature alloys based on NiAl-(Cr,Mo), Metals 10 (7) (2020) 1–14, doi:10.3390/met10070961.